Characterization and modelling of a carbon ramming mix used in high temperature industry

J. Brulin, Amna Rekik, L. Josserand, Eric Blond, Alain Gasser, F. Roulet

Characterization and modelling of a carbon ramming mix used in high-temperature industry

J. Brulin[a,b], A. Rekik[a], L. Josserand[a], E. Blond[a], A. Gasser[a], F. Roulet[b]

[a]*Institut PRISME (EA 4229, University of Orléans), Polytech'Orléans*
8, rue Léonard de Vinci, 45072 Orléans, France
[b]*Saint-Gobain CREE, 550, avenue Alphonse Jauffret, BP 224, 84306 Cavaillon, France*

Abstract

This paper is devoted to the modelling of a specific ramming mix mainly used in the high-temperature industry due to its high-compacting behaviour. This material has the ability to absorb the deformation of parts submitted to high thermal loads. Triaxial tests were carried out in order to identify the shear behaviour and an instrumented die compaction test was developed for the hardening behaviour identification. Tests on the ramming mix were lead for a temperature range between 20°C and 80°C. The temperature effect is particularly observed on the material response when compacted. The main features of the behaviour of the ramming mix can be represented by the theoretical framework of the Modified Cam-Clay model. A single variable allows to accurately reproduce the hardening behaviour depending on temperature. Moreover an extension of the model for the hardening behaviour at high pressures is proposed. A good agreement between the experimental data and numerical tests is reached with this model.

Keywords: ramming mix, parameters identification, die compaction test, triaxial test, temperature effect, finite element, Modified Cam-Clay model

1. Introduction

The steel industry requires huge structures mainly composed of refractory materials. The thermomechanical properties of these materials perfectly suit high temperature applications. However, the expansion of these constituents can damage some parts of the structure. To avoid this damage, ramming mixes are often used to absorb the deformations. Indeed, these loose materials are well-known for their high-compacting behaviour. An appropriate modelling of this material must at least be able to reproduce the compaction behaviour sensitive to the temperature effect.

This paper investigates the case of a ramming mix composed of graphite (80%) and coal tar (20%). Its aspect can be compared with a bituminous sand. In the literature, many studies were carried out in order to predict the behaviour of loose geological materials (Bousshine et al., 2001; Liu and Carter, 2002), pharmaceutical powders (Wu et al., 2005; Han et al., 2008) or metallic powders (Park et al., 1999; Chtourou et al., 2002). The modelling of the loose materials whose behaviour is highly dependent on the porosity rate is classically based on micro-mechanical and macro-mechanical approaches. The first one assumes that each particle is a sphere. It takes also into account the contact interactions between the particles (Helle et al., 1985; Fleck et al., 1992; Biba et al., 1993; Fleck, 1995). From a discrete approach, the macroscopic behaviour of a material can be evaluated by means of homogenization methods (Piat et al., 2004; Le et al., 2008). Although micro-mechanical models are devoted to understand the physical behaviour of the constituents, macro-mechanical models (Shima and Oyane, 1976; Gurson, 1977; Haggblad, 1991) are well-adapted for engineering applications which often occur at a

2

large scale. The phenomenological models were mainly developed for applications in soil mechanics, such as the Drucker-Prager Cap model (Drucker and Prager, 1952), the Modified Cam-Clay model (Roscoe and Burland, 1968) or the Di Maggio-Sandler model (Di Maggio and Sandler, 1971). These Cap models allow to reproduce the hardening behaviour in compaction of initially loose powders. In the same approach, many extensions of these models for porous materials were developed (Chtourou et al., 2002; Aubertin and Li, 2004; Khoei and Azami, 2005; Park, 2007). The Drucker-Prager Cap model remains one of the most used due to its ability to reproduce shearing and compaction behaviours. The parameters of this model are simply identified by carrying classical tests. The hardening behaviour is described by a Cap parameter dependent on the volumetric inelastic strain (Doremus et al., 2001; Wu et al., 2005). In these studies, Young's modulus and Poisson's ratio defining the elastic part are assumed to be constant. In order to reproduce a possible nonlinear elastic behaviour, some authors have chosen to identify elastic parameters and yield surface parameters evolving with the relative density (Kim et al., 2000; Sinka et al., 2003; Michrafy et al., 2004; Han et al., 2008). The influence of the temperature on the parameters of a Drucker-Prager Cap model was rarely taken into account (Piret et al., 2004). The thermal effects were mainly studied in the geotechnical field.

Models inspired on the Modified Cam-Clay model are often used to reproduce the behaviour of soils such as clays (Liu and Carter, 2002; Piccolroaz et al., 2006). It is an elastoplastic model with a yield surface which can grow or shrink according to the hardening rule. Triaxial and die compaction tests are widely used to identify the shearing and hardening behaviours. The

3

hardening behaviour of the material is written in a specific space in which only two constant parameters are used to define nonlinear elastic and plastic parts. Furthermore, this model was extended in order to take into account the temperature effects (Hueckel and Borsetto, 1990; Hueckel and Baldi, 1990; Tanaka et al., 1995; Sultan et al., 2002) which mainly modify the size of the yield surface. In the Modified Cam-Clay model, the size of the yield surface follows the evolution of the yield stress under hydrostatic compression p_c. According to the extensions of the Modified Cam-Clay model, this evolution can be of exponential or polynomial form with various parameters to identify. For these reasons, the Modified Cam-Clay model was chosen in this work in order to reproduce the shearing and hardening behaviours of the ramming mix sensitive to the temperature effect. No tensile strength, nor cohesion are introduced in this model due to the context of the study mainly focused on the compacting behaviour.

This paper is organised as follows. Section 2 presents the triaxial and die compaction tests performed on ramming mix samples with cylindrical shape allowing the investigation of the shearing and hardening behaviours at different temperatures. A specific calibration step is carried out to know the radial stress exerted on the sample during the die compaction test. Section 3 describes the adopted Modified Cam-Clay model. Only one parameter is used to modify the size of the yield surface in order to reproduce the temperature effect. An extension of this model to high-compressive pressures is also introduced. The various parameters of this model are identified from the triaxial and die compaction tests data. Finally in section 4, the choice of the Modified Cam-Clay model is first confirmed by comparison of the nu-

merical predictions to experimental data obtained from the tests used for the identification of the model parameters. Then, a hydrostatic compression test at room temperature and a die compaction test with heating validate the ability of this model to reproduce the behaviour of the studied ramming mix.

2. Characterization of the ramming mix behaviour: triaxial and die compaction tests

In the high-temperature industry, the ramming mix is used to protect the steel shell from the expansion of the refractory bricks. Located between the shell and the bricks, the ramming mix is not directly subjected to the thermal load applied on the masonry. It is mainly stressed in compression at low strain rates for a temperature range between 20°C and 80°C. Triaxial and die compaction tests are carried out to identify the shearing and hardening behaviours at different temperatures and strain rates. The three-dimensionnal stress state is defined by two invariants: the equivalent pressure stress p and the von Mises equivalent stress q. They are defined as follows:

$$p = -\frac{1}{3}\text{trace}(\underline{\underline{\sigma}}) \tag{1}$$

$$q = \sqrt{\frac{3}{2}\underline{\underline{S}} : \underline{\underline{S}}} \tag{2}$$

where $\underline{\underline{S}}$ is the deviatoric part of the stress tensor $\underline{\underline{\sigma}}$, expressed as follows:

$$\underline{\underline{S}} = \underline{\underline{\sigma}} + p\underline{\underline{I}} \tag{3}$$

$\underline{\underline{I}}$ is the second order identity tensor.

5

In the case of a cylindrical sample submitted to a compressive axial stress ($\sigma_A < 0$) and a compressive radial stress ($\sigma_R < 0$), the equivalent pressure stress reads:

$$p = -\frac{\sigma_A + 2\sigma_R}{3} \tag{4}$$

and, the von Mises equivalent stress is:

$$q = |\sigma_A - \sigma_R| \tag{5}$$

2.1. Characterization of the shearing behaviour: triaxial tests

Hereafter, we will describe the testing system required to carry out triaxial tests on the ramming mix. The aim is to characterize the shearing behaviour of this material. Figure 1 depicts the triaxial compression apparatus used to perform the triaxial tests. This apparatus is composed of a cell of a 3.5 MPa capacity, a pressure controller, a 25 mm LVDT sensor and a 10 kN load cell. The cell is filled with water in order to apply a controlled radial stress on the sample. This cell is axially free. The axial displacement of the cell which is measured by the LVDT sensor corresponds to the axial dispacement of the lower part of the sample. The upper part of the sample is motionless which yields to the axial compression of the sample. The axial force is measured by the load cell. This testing system ensures that cylindrical samples are submitted to axial loads under a constant radial pressure imposed by the water present inside the cell as shown in figure 1.

2.1.1. Triaxial test procedure

The tested samples are 50 mm in diameter and 95 mm in height. Each specimen is obtained by a manual precompaction of 240 g of carbon ramming

6

mix into a die, up to an average void ratio e of 0.42 ± 0.08 where e is given as follows:

$$e = \frac{\rho_r V}{m} - 1 \qquad (6)$$

ρ_r is the real density of the material, m and V are the mass and the volume of the sample, respectively. For this material, a gas pycnometer test would be the most appropriate for the determination of the real density. Here, the measured real density is $\rho_r = 1820$ kg/m³. This value is provided by the Le Chatelier densimeter test which consists in the immersion of the ramming mix in oil. Water was avoided to allow a better mixture with the coal tar. With this apparatus, it is impossible to apply a pressure which could favor the filling of all the voids by the oil. These voids are located between graphite grains and coal tar and also in the graphite grains. This grain porosity is the most complicated to fill by the oil. A mercury porosimetry on the graphite grains shows there are two kinds of porosities:

- a grain macroporosity with an average void ratio of 4 μm,

- a grain microporosity with an average void ratio of 0.02 μm.

A simple relation used in porosimetry tests allow to link the pressure P exerted on the liquid to fill the voids and the average diameter d of the voids:

$$P = \frac{|4\gamma cos(\alpha)|}{d} \qquad (7)$$

where γ is the interfacial tension and α is the wetting angle between the liquid and the surface of the sample. Considering oil for liquid in the densimeter test with γ=0.03 N/m and α=30°, the grain macroporosity is filled

7

with a pressure of 0.025 MPa (lower than the atmospheric pressure) although 5 MPa are required to fill the grain microporosity. So, only the open macroporosity in and between grains is filled with the Le Chatelier densimeter test and so taken into account in the real density measurement. We will consider a macro void ratio e.

In the case of the triaxial test, the initial macro void ratio of the sample is heterogeneous due to a manual compaction mode. This sample is set into an elastomer film to prevent the penetration of water. During the triaxial test, the sample is first submitted to a constant hydrostatic pressure $p = -\sigma_R$. Then, the axial displacement of the cell at constant velocity and radial pressure implies the increase of the axial stress on the sample following a stress path defined by the linear relation $q = 3p$ between the stress invariants.

2.1.2. Triaxial test results: temperature and strain rate effects

At room temperature, triaxial tests were carried out for confining pressures from 100 kPa to 800 kPa with velocities of 0.1 mm/min, 0.5 mm/min and 1 mm/min. To study the influence of the temperature on the shearing behaviour, a triaxial apparatus operating at high temperatures as used by Olmo et al. (1996) is necessary. The triaxial apparatus of this study has no available heating control, therefore a specific procedure was followed. The sample is first preheated during two hours, at for example 50°C, it is then set on the triaxial apparatus. In a second step, the cell is filled with preheated water at 50°C. In order to minimize the decrease of temperature during the test, a velocity of 1 mm/min was chosen for the triaxial tests at 50°C and 80°C. The strain rate effect is so not considered at elevated temperatures. For each triaxial test, a critical shearing stress is reached when the increase

8

of the von Mises equivalent stress stops. As presented in figure 2 for triaxial tests with a confining pressure of 200 kPa, no effect of the strain rate was observed at room temperature. Only the temperature has an influence on the critical shearing stress which decreases.

2.2. Characterization of the hardening behaviour: die compaction tests

A hydrostatic compression test is classically used to identify the hardening behaviour of porous materials. An œdometer test on a confined cylindrical sample constitutes also an acceptable solution but requires to be instrumented in order to measure both axial and radial stresses applied on the sample. The axial stress is easy to get due to a load cell located on the apparatus, whereas the radial stress is applied by the confinement of a hollow cylinder. In some cases, it is possible to dispose of a load sensor located in the die in order to have a direct measure (Mesbah et al., 1999; Sinka et al., 2003). Otherwise, simple relations can be established between the external circumferential strain of the hollow cylinder and the radial stress applied on the sample. The identification of this calibration relation is detailed in the next paragraph.

An instrumented die compaction test on a static press INSTRON 5800R was developed as presented in figure 3. Axial displacement and axial load are acquired with a 50 mm LVDT sensor and a 250 kN load cell, respectively. Thanks to a heating control system, compaction tests at elevated temperature are possible. A heating collar with an integrated K-type thermocouple linked to the thermal control is set around the free cylinder. A water-cooling system is added between the load cell and the upper piston in order to avoid the expansion of the load cell during these tests which could affect the mea-

9

surement. Moreover, a double-effect compaction is chosen (free die in the axial direction) to compress equally the sample at the top and the bottom. The die/sample interface is lubricated with a silicon grease to homogenize the radial stresses applied on the height of the sample. The friction coefficient between the final compacted sample and the lubricated die was taken to be 0.22 measured with an inclined plane apparatus. This value is an estimation of the friction coefficient which evolves (decreases globally) when the sample is compacted due to the decrease of the roughness of the lateral area of the ramming mix sample. Finally, 8 circumferential gauges are set around the die in order to evaluate its average circumferential strain. These gauges are located at mid-height of the die with 70 mm between the lowest and the highest ones. They allow to record strains of the die for samples higher than 70 mm.

2.2.1. Calibration test on a rubbery sample

The calibration relation can be identified experimentally from a test on an incompressible rubbery sample (Mosbah et al., 1997; Geindreau et al., 1999; Hong et al., 2008; Michrafy et al., 2009) or numerically when the circumferential strain of the hollow cylinder is known (Bier et al., 2007). The calibration test with an incompressible sample is here selected. It is worth noting that for an incompressible rubbery sample submitted to a confined load, there is an equality between the axial and radial stresses. In this case, it is possible to identify a linear relation between the applied hydrostatic pressure P and the average of the circumferential strains $\varepsilon_{\theta\theta}^{die}$ measured by

10

gauges as follows:

$$C(H_{sample}) = \frac{P}{\varepsilon_{\theta\theta}^{die}} \tag{8}$$

$C(H_{sample})$ is the seeked function which can depend on the height of the sample. Figure 4 illustrates the evolution of $\frac{P}{\varepsilon_{\theta\theta}^{die}}$ as a function of the height of the sample. Eight die compaction tests show a constant value for the C parameter when the contact between the die and the sample is established. These tests carried out on rubbery samples of 102 mm in height (6 tests) and 92 mm in height (2 tests) allow to identify the following value for C:

$$C_{test} = 51 \ GPa \tag{9}$$

The experimental value can be compared with the theoretical value obtained for the case of a hollow cylinder with a height L, an internal and an external radius R_1 and R_2, respectively. The behaviour of the cylinder is assumed to be linear elastic with a Young's modulus E and a Poisson's ratio ν. When this cylinder is submitted to an internal pressure p_1, the local stress field (Salençon, 2007) is given by:

$$\sigma_{rr} = \frac{p_1 R_1^2}{R_2^2 - R_1^2} \left(1 - \left(\frac{R_2}{r} \right)^2 \right) \tag{10}$$

$$\sigma_{\theta\theta} = \frac{p_1 R_1^2}{R_2^2 - R_1^2} \left(1 + \left(\frac{R_2}{r} \right)^2 \right) \tag{11}$$

where r is the local radius ($R_1 \leq r \leq R_2$). Then, taking into account the boundary conditions:

$$\sigma_{rr}(r = R_2) = 0 \tag{12}$$

and:

$$\sigma_{\theta\theta}(r = R_2) = \frac{2p_1 R_1^2}{R_2^2 - R_1^2} \tag{13}$$

Moreover, the constitutive local Hooke's law gives:

$$\varepsilon_{\theta\theta} = \frac{1}{E}\sigma_{\theta\theta} - \frac{\nu}{E}(\sigma_{rr} + \sigma_{zz}) \tag{14}$$

It is possible to rewrite equation (14) for $r = R_2$:

$$\sigma_{\theta\theta}(r = R_2) = E\varepsilon_{\theta\theta}(r = R_2) + \nu\sigma_{zz}(r = R_2) \tag{15}$$

In this theoretical result, the friction between the sample and the cylinder which induces an axial stress of the cylinder is not taken into account. We only consider that the upper and lower sections of the steel cylinder are free which leads to (Salençon, 2007):

$$\sigma_{zz} = 0 \tag{16}$$

and so:

$$\sigma_{\theta\theta}(r = R_2) = E\varepsilon_{\theta\theta}(r = R_2) \tag{17}$$

Finally, combining equations (13) and (17), we can deduce:

$$C_{theory} = \frac{p_1}{\varepsilon_{\theta\theta}(r = R_2)} = \frac{E}{2}\left(\left(\frac{R_2}{R_1}\right)^2 - 1\right) \tag{18}$$

For the considered die: $R_1 = 40.6$ mm, $R_2 = 50$ mm and $E = 210$ GPa. The theoretical constant can be evaluated:

$$C_{theory} = 54 \ GPa \tag{19}$$

The 6% deviation with the experimental result is due to the friction neglect. This theoretical value validates the identified experimental one. As a conclusion, this calibration step allows to estimate the average radial stress of the ramming mix sample during a die compaction test.

12

2.2.2. Die compaction tests at different temperatures and strain rates

For the compaction tests, 700 g of carbon ramming mix are poured into a die and precompacted with the apparatus up to an initial macro void ratio of 0.37 ± 0.08. The precompaction step induces an axial force close to 1 kN and a radial stress which allows to maintain the mid-height of the free cylinder aligned with the mid-height of the initial sample. The initial sample is 81 mm in diameter and 102 mm in height which gives an aspect ratio higher than 1 as mentioned in Doremus et al. (2001) in order to minimize the stress gradients in the sample. This ratio and the double-effect compaction system allow to assume that the initial macro void ratio is homogeneous. For tests at elevated temperature, strains are recorded during heating and dwell time in order to take the expansion into account. Load/unload cycles are programmed to identify both elastic and plastic parts of the hardening behaviour. Results of these cycles at different temperatures (20°C, 50°C and 80°C) and velocities (0.1 mm/min and 1 mm/min) are presented in figure 5. The two curves corresponding to the tests at room temperature at rates of 0.1 mm/min and 1 mm/min are very close. In the same way, the two curves at a temperature of 50°C merge. The strain rate has no effect on the hardening behaviour. The repeatability of the die compaction test is checked at 80°C and 1 mm/min. Only the temperature seems to have an influence on the hardening behaviour. For the same consolidation state, the axial load decreases with the temperature. This phenomenon is observed in figure 6 where the hardening behaviour with heating is compared with the one at room temperature. In this test, the sample has an initial macro void ratio of 0.34 ± 0.08 and the velocity is 0.4 mm/min. During the test, a first

heating from 20°C to 50°C and a second one from 50°C to 80°C are imposed at 3°C/h on the external part of the steel cylinder. Due to the viscous part of the ramming mix, the increase of temperature induces a slight softening of the axial stress during a die compaction test.

2.2.3. Die compaction tests at high pressures

Figure 7 presents the results of a die compaction test carried out up to high pressures (40 MPa) at room temperature. The first part of the curve showing the load/displacement diagram is similar to the plastic part of the hardening behaviour at room temperature presented in figure 5. In fact, until a 27 mm axial displacement, the macro void ratio is positive and all the macro voids in and between the particles are progressively closed. Afterwards due to pressures higher than 4 MPa, the microporosity of the graphite grains is filled by the coal tar. Considering equation (7) with γ=0.03 N/m and α=30° which are the parameters for a bituminous, a pressure close to 4 MPa is obtained in order to fill the microporosity of the graphite grains. The macro void ratio is negative because the real density does not account for this microporosity.

As done for the Modified Cam-Clay model, the hardening behaviour is written in the $(ln(p),\ e)$ plane. In figure 8 are depicted the results of the die compaction tests carried out at room temperature under low and high pressures. It allows to illustrate how only one elastic slope and two plastic slopes describe the hardening behaviour of the ramming mix. The formulation of an extended Modified Cam-Clay model is presented in the following section.

14

3. Modelling of the ramming mix

3.1. Modified Cam-Clay formulation

For its ability to reproduce the elastic and plastic parts of the hardening behaviour with slopes and the temperature effect, the Modified Cam-Clay model implemented in the finite element software ABAQUS/Standard (Abaqus, 2007) is used as the basis of the proposed model. It is an extension of the original model developed by Roscoe and Burland (1968) introducing the critical state concept.

3.1.1. Yield surface of the model

The Modified Cam-Clay model described in figure 9 is based on a yield surface with an associated flow rule:

$$F = \frac{1}{\beta^2}\left(\frac{p}{a} - 1\right)^2 + \left(\frac{q}{Ma}\right)^2 - 1 = 0 \tag{20}$$

where M is a constant that defines the slope of the critical state line, a is the size of the yield surface and β is a constant which can modify the shape of the cap. This parameter is here used to take into account the temperature effect on the yield surface of the hardening behaviour. It is worth noting that for a hydrostatic compression p_c, the yield stress is given by:

$$p_c(T) = a(1 + \beta(T)) \tag{21}$$

The yield surface (equation (20)) is written in terms of two stress invariants: the equivalent pressure stress p and the von Mises equivalent stress q. In this section, we introduce some notations. The strain tensor $\underline{\underline{\varepsilon}}$ is decomposed in two parts as follows:

$$\underline{\underline{\varepsilon}} = \underline{\underline{\varepsilon}}^{el} + \underline{\underline{\varepsilon}}^{pl} \tag{22}$$

15

$\underline{\underline{\varepsilon}}^{el}$ denotes the elastic part of the strain and $\underline{\underline{\varepsilon}}^{pl}$ represents its plastic part. Each of these strains can be divided into deviatoric and volumetric parts. The strain field (equation (22)) reads then:

$$\underline{\underline{\varepsilon}} = (\underline{\underline{\varepsilon}}^{el}_{dev} + \underline{\underline{\varepsilon}}^{pl}_{dev}) - (\varepsilon^{el}_{vol} + \varepsilon^{pl}_{vol})\underline{\underline{I}} \tag{23}$$

Moreover, the volumetric part of the strain field ε_{vol} can be expressed as a function of the macro void ratio e and the initial macro void ratio e_0:

$$\varepsilon_{vol} = \varepsilon^{el}_{vol} + \varepsilon^{pl}_{vol} = ln\left(\frac{1+e}{1+e_0}\right) \tag{24}$$

The strain field will evolve following a hardening behaviour for high p values and a shearing behaviour for high q values.

3.1.2. Shearing behaviour

The critical state line is the key point of the model because it allows to define hardening and softening behaviours of the material. In fact, when submitted to an increasing deviatoric stress for a constant value of p lower than a, the material exhibits a deviatoric elastic behaviour defined by:

$$d\underline{\underline{S}} = 2G d\underline{\underline{\varepsilon}}^{el}_{dev} \tag{25}$$

where G is the shear modulus whose expression is defined by:

$$G = \frac{3(1-2\nu)(1+e_0)}{2(1+\nu)\kappa} \exp(\varepsilon^{el}_{vol})p \tag{26}$$

κ is the logarithmic bulk modulus. Equation (26) demonstrates that G increases as the material is compacted. Then, the yield surface is reached for values of q upper than the product Mp leading to a softening behaviour. The yield stress curve decreases and reaches the critical state line.

16

3.1.3. Hardening behaviour

When submitted to hydrostatic pressures, the elastic part is governed by the volumetric behaviour of the material as follows:

$$\exp(\varepsilon_{vol}^{el}) = 1 + \frac{\kappa}{1 + e_0} \ln \frac{p_0}{p} \tag{27}$$

where p_0 is the initial value of the equivalent pressure stress. If yielding occurs, the material exhibits a hardening behaviour described in figure 10 and defined as:

$$de = -\lambda d(\ln p) \tag{28}$$

λ is the logarithmic hardening constant for the plasticity. Hereafter, this slope takes the value of λ_1 for positive macro void ratios and λ_2 for negative macro void ratios. The hardening behaviour was implemented thanks to a user defined field (USDFLD) subroutine which computes the macro void ratio of each element constituting the mesh. Then, two specific logarithmic hardening constants function of the macro void ratio are defined. The hardening behaviour is characterized by the growth of the yield surface size defined by:

$$a = a_0 \exp \left[(1 + e_0) \frac{1 - \exp(\varepsilon_{vol}^{pl})}{\lambda - \kappa \exp(\varepsilon_{vol}^{pl})} \right] \tag{29}$$

where a_0 is the initial position of a. This initial overconsolidation is computed as follows:

$$a_0 = \frac{1}{2} \exp \left(\frac{e_1 - e_0 - \kappa \ln p_0}{\lambda - \kappa} \right) \tag{30}$$

e_1 denotes the macro void ratio of the ramming mix for a hydrostatic pressure of 1 MPa. If the critical state line is reached after the yielding, the material then distorts without any changes in shear stress or volume.

17

355   Finally, the use of the Modified Cam-Clay model requires 9 parameters:

356   • ν and κ for the elastic behaviour,

357   • λ_1 and λ_2 for the plastic behaviour,

358   • M for the critical state line,

359   • β for the yield surface evolving with the temperature,

360   • e_0, e_1 and p_0 to define the initial state of the material.

361 *3.2. Parameters identification*

362   For different temperatures, the shearing parameter M is identified from
363 the triaxial tests carried out and described in section 2.1.2. Results of the
364 die compaction tests (section 2.2.2) written in the $(ln(p),\ e)$ plane allow to
365 obtain the parameters of the hardening behaviour. The temperature effect
366 on the parameters of this model is particularly observed.

367 *3.2.1. The critical state line*

368   From the results of the triaxial tests mentionned in section 2.1.2, the
369 critical shearing stresses permit to plot the critical state line. Considering no
370 effect of the velocity, a single value of M was identified at room temperature:
371 $M_{20°C} = 1.18$ as presented in figure 11. Results of tests carried out at 50°C
372 and 80°C are depicted in the same figure. All of them are located under the
373 critical state line identified at room temperature. Since there is no thermal
374 control during these tests, we can only conclude the global influence of the
375 temperature on the slope of the critical state line but nothing on the real
376 value of the parameter M. For this reason, a slight decrease of the slope was
377 assumed for this range of temperatures: $M_{50-80°C} = 1.1$.

18

3.2.2. Parameters of the hardening behaviour

Parameters identification is done in the $(ln(p), e)$ plane as previously ex-
plained. Results of the carried die compaction tests at different temperatures
are exploited as in figure 8. The parameters of the hardening behaviour are
reported in table 1. Temperature has no effect on the elastic and plastic
slopes. As shown in figure 12, only the parameter e_1 decreases with the in-
crease of the temperature. It means that for the same hydrostatic pressure
(1 MPa), the sample is more compacted at 80°C than at 20°C. This result is
directly related to a phenomenon often observed (Hueckel and Baldi, 1990;
Sultan et al., 2002): the decrease of the yield surface with respect to the
temperature. As written in equation (30), e_1 is only used to compute the ini-
tial consolidation state at the corresponding temperature. In this paper, the
temperature effect is reproduced with the parameter β which can modify the
shape of the cap part. A unit value is set at room temperature: $\beta(20°C) = 1$.
In order to assess $\beta(50°C)$ and $\beta(80°C)$, we consider a hydrostatically com-
pacted sample heated from the room temperature up to a temperature T
without any volume change. It means that during this heating step the con-
solidation state a and the void ratio e remain constant. From equation (21),
we can write:

$$\beta(T) = \frac{p_c(T)}{a(T)} - 1 \tag{31}$$

At room temperature:

$$\beta(20°C) = \frac{p_c(20°C)}{a(20°C)} - 1 = 1 \tag{32}$$

19

Considering the constant consolidation state, it comes at higher temperatures:

$$\beta(T) = \frac{p_c(T)}{a(20°C)} - 1 = 2\frac{p_c(T)}{p_c(20°C)} - 1 \tag{33}$$

Equation (28) and the knowledge of parameters e_1, λ_1, λ_2 reported in table 1 allow to compute the values $p_c(50°C)$ and $p_c(80°C)$ from a chosen value of $p_c(20°C)$ after heating without any volume change. The computation of β (equation (33)) provides the following values at 50°C and 80°C:

$$\beta(50°C) = 0.56 \quad \text{and} \quad \beta(80°C) = 0.21 \tag{34}$$

All the parameters needed for the computation of the Modified Cam-Clay model for the ramming mix are presented in table 2. The Poisson's ratio ν is set equal to a classical value of 0.25. The obtained results are in agreement with the tendencies of the evolution of the Cam-Clay parameters with temperature as mentionned in Graham et al. (2001). In fact, heating produces variations of the yield surface size leading to a decrease of the elastic zone.

4. Numerical results

Axisymmetric numerical analysis of triaxial and die compaction tests used for parameters identification is carried out with the finite element code ABAQUS/Standard 6.7. Two additional tests independent from the previous ones are also modelled in order to validate the model. For all these simulations, the ramming mix behaviour is defined with the parameters previously identified.

20

4.1. Modelling of identification tests

To simulate triaxial and compaction tests, the ramming mix sample is meshed with four-node axisymmetric continuum elements. Upper and lower pistons are modelled with rigid supports.

4.1.1. Triaxial tests

For the triaxial test, a hard-contact condition in normal behaviour and a friction coefficient of 0.3 (measured with an inclined plane apparatus between the filter paper and the ramming mix) in tangential behaviour is defined between the sample and pistons. Due to the manual compaction mode, an initial heterogeneous macro void ratio is considered for the sample with an average value of 0.42. The heterogeneous distribution of the macro void ratio is assumed to be linear with $e = 0.52$ at the bottom of the sample and $e = 0.32$ at its top. In fact, the initial sample is more compacted in its upper part in order to respect the chosen initial height. This distribution was chosen due to its efficiency to accurately reproduce the shearing behaviour under a radial stress of 100 kPa. As shown in figure 13(a), the sample is first hydrostatically stressed on its upper and lateral areas. Then, an axial displacement is imposed on the lower piston. The axial load is read on the upper piston which is locked. This load corresponds to the one measured by the load cell in figure 1. In fact for the simulation, the axial pressure exerted by water is directly applied on the sample and not on the upper piston. When compacted, the sample takes a convex shape (see figure 13(b)) and is mainly stressed in the center and the corners. Numerical and experimental results compare the evolution of the axial load with respect to the axial displacement. They are shown in figure 14 at room temperature and in figure 15 at higher

temperatures (50°C and 80°C). A good agreement is reached between tests and simulations for the shearing behaviour.

4.1.2. Die compaction tests

In the die compaction test modelling presented in figure 16(a), the steel die is meshed with four-node axisymmetric continuum elements. Its behaviour is assumed to be isotropic elastic linear with a Young's modulus $E = 210$ GPa and a Poisson's ratio $\nu = 0.3$. Contact conditions are defined between the steel parts and the sample: a hard-contact condition in normal behaviour and a friction coefficient of 0.22 in tangential behaviour as explained in section 2.2. Due to the double-effect precompaction step, a homogeneous macro void ratio of 0.37 describes the initial state of the sample. It is submitted to an axial displacement imposed by the lower piston. The upper piston is locked and provides the axial load applied on the sample. As shown in figure 16(b), the radial stress distribution in the sample is globally homogeneous. Moreover, the steel die which axially moves up due to the friction, is radially stressed in compression where it is in contact with the sample and in tensile elsewhere. The axial load response to the axial imposed displacement is studied. As shown in figure 17, elastic and plastic parts of the hardening behaviour accurately fit with the proposed model at room temperature. The same agreement between experimental and numerical results is obtained as well at 50°C and 80°C. Figure 18 shows the necessity to allow for a second plastic slope λ_2 because it permits to define the hardening behaviour at high pressures. In order to avoid numerical problems, a sweet transition is defined between the two plastic slopes.

22

4.2. Validation of the model

4.2.1. Die compaction test with loads/unloads and heating

The first test used for the validation is a die compaction test with load/unload cycles and heating during the test. A sample with an initial homogeneous macro void ratio of 0.37 is submitted to a load/unload cycle at a velocity of 0.2 mm/min and an increase of the temperature in two steps: first from 20°C to 50°C and then from 50°C to 80°C as shown in figure 19. This thermal field was measured by the thermocouple during the test and applied in the simulation on the external part of the free cylinder. Thanks to a preliminary thermal computation in transient state with the material properties defined in table 3, the evolution of the temperature in the ramming mix sample is known. Numerical and experimental results for this test are depicted in figure 20. The efficiency of the model to reproduce accurately the hardening behaviour of the material evolving with the temperature is validated.

4.2.2. Hydrostatic compression test

A second test using the triaxial apparatus is developped as well. The idea is to carry out a hydrostatic compression test with loads and unloads, with the only use of the pressure exerted by water. For the ramming mix sample preparation, a similar procedure to that described for triaxial tests was adopted. As shown in figure 21, the cell is axially locked like the upper piston which has no contact with the sample. So no axial displacement is applied on the sample and no axial load is measured by the load cell. The sample is put on the lower locked piston and a cylindrical part is set above in order to attach the elastomer film. The sample is then hydrostatically stressed on the lateral and upper surfaces. In order to evaluate the way

23

the sample distorts, the axial displacement of the center of the cylindrical part above the sample is investigated. The sample being in the cell filled with water, a direct measurement is impossible. For this reason a marker tracking method (Nugent et al., 2000; Lee et al., 2009) is chosen. Markers are drawn on the cylindrical part. A 8-bit CCD camera allows to grab images of the marked area for each hydrostatic stress increment of 50 kPa. The displacement field of the center of the cylindrical part can be computed. We assume that this displacement corresponds to the one of the upper part of the sample. Figure 22 shows the experimental and numerical evolution of the axial displacement of the upper part of the sample with the hydrostatic stress. The plastic part is well-reproduced although the elastic part observed is not accurately numerically obtained. It is due to the fact that during the unload, the cylindrical part goes up and loses the contact with the upper part of the sample. It means that the axial displacement of the cylindrical part is different from the axial displacement of the upper part of the sample at the end of the unload. Moreover during the unload, a pump-effect leads to the filling of the space between the cylindrical part and the upper part of the sample with air. So during the reload, the air is first evacuated and then the sample loaded. This phenomenon is not numerically taken into account which leads to slight differences for the elastic part.

5. Conclusion

In the present paper, a specific ramming mix of the steel industry was studied in order to select an appropriate model reproducing its behaviour. A macroscopic model which is well adapted to engineering applications was

24

retained. It is the Modified Cam-Clay model which is often used in the geotechnical field due to its ability to reproduce the shearing and hardening behaviours. In the proposed model, a single parameter β permits to take into account the temperature effect on the hardening behaviour. Moreover, the hardening behaviour was completed for high pressures defining a second plastic slope. This second slope is related to the microporosity filling. An experimental campaign was lead to determine the material parameters of the proposed model. Triaxial tests allowed to identify the slope of the critical state line of the model and an instrumented die compaction test was conceived to characterize the hardening behaviour. For all these tests, no influence of the strain rate was established for strain rates lower than $2 \times 10^{-4}\ \mathrm{s}^{-1}$. Only the temperature effect on the critical state line and the yield surface was clearly observed. In fact, the size of the yield surface decreases while temperature increases. In order to validate the agreement reached between experimental and numerical results, two additional tests were carried out. A die compaction test with heating and a hydrostatic compression test at room temperature coupled with a marker tracking method have confirmed the relevance of the model to reproduce the behaviour of the ramming mix.

25

Abaqus, 2007. Abaqus Standard Reference Manuals, version 6.7. Simulia, Providence, RI, USA.

Aubertin, M., Li, L., 2004. A porosity-dependent inelastic criterion for engineering materials. International Journal of Plasticity 20 (12), 2179–2208.

Biba, N., Keife, H., Stahlberg, U., 1993. A finite-element simulation of powder compaction confirmed by model-material experiments. Journal of Materials Processing Technology 36 (2), 141–155.

Bier, W., Dariel, M., Frage, N., Hartmann, S., Michailov, O., 2007. Die compaction of copper powder designed for material parameter identification. International Journal of Mechanical Sciences 49 (6), 766–777.

Bousshine, L., Chaaba, A., de Saxcé, G., 2001. Softening in stress-strain curve for Drucker-Prager non-associated plasticity. International Journal of Plasticity 17 (1), 21–46.

Chtourou, H., Guillot, M., Gakwaya, A., 2002. Modeling of the metal powder compaction process using the cap model. Part I. Experimental material characterization and validation. International Journal of Solids and Structures 39 (4), 1059–1075.

Di Maggio, F., Sandler, I., 1971. Material model for granular soils. Journal of the Engineering Mechanics Division 97 (3), 935–950.

Doremus, P., Toussaint, F., Alvain, O., 2001. Simple tests and standard procedure for the characterisation of green compacted powder. A. Zavaliangos and A. Laptev (eds.), Recent Developments in Computer Modelling of Powder Metallurgy Processes, IOS Press, Amsterdam, 29–41.

26

Drucker, D. C., Prager, W., 1952. Soil mechanics and plastic analysis on limit design. Quarterly of Applied Mathematics 10(2), 157–165.

Fleck, N. A., 1995. On the cold compaction of powders. Journal of the Mechanics and Physics of Solids 43 (9), 1409–1431.

Fleck, N. A., Kuhn, L. T., McMeeking, R. M., 1992. Yielding of metal powder bonded by isolated contacts. Journal of the Mechanics and Physics of Solids 40 (5), 1139–1162.

Geindreau, C., Bouvard, D., Doremus, P., 1999. Constitutive behaviour of metal powder during hot forming. Part I: Experimental investigation with lead powder as a simulation material. European Journal of Mechanics - A/Solids 18, 581–596.

Graham, J., Tanaka, N., Crilly, T., Alfaro, M., 2001. Modified Cam-Clay modelling of temperature effects in clays. Canadian geotechnical journal 38, 608–621.

Gurson, A. L., 1977. Continuum theory of ductile rupture by void nucleation and growth, I. Yield criteria and flow rules for porous ductile media. Journal of Engineering Materials and Technology-Transactions of the ASME 99 (1), 2–15.

Han, L., Elliott, J., Bentham, A., Mills, A., Amidon, G., Hancock, B., 2008. A modified Drucker-Prager Cap model for die compaction simulation of pharmaceutical powders. International Journal of Solids and Structures 45 (10), 3088–3106.

27

Helle, A., Easterling, K., Ashby, M., 1985. Hot-isostatic pressing diagrams: New developments. Acta Metallurgica 33, 2163–2174.

Haggblad, H. A., 1991. Constitutive models for powder materials. Powder Technology 67 (2), 127–137.

Hong, S.-T., Hovanski, Y., Lavender, C. A., Weil, K. S., 2008. Investigation of die stress profiles during powder compaction using instrumented die. Journal of Materials Engineering and Performance 17 (3), 382–386.

Hueckel, T., Baldi, G., 1990. Thermoplasticity of saturated clays: Experimental constitutive study. Journal of Geotechnical Engineering 116 (12), 1778–1796.

Hueckel, T., Borsetto, M., 1990. Thermoplasticity of saturated soils and shales: Constitutive equations. Journal of Geotechnical Engineering 116 (12), 1765–1777.

Khoei, A., Azami, A., 2005. A single cone-cap plasticity with an isotropic hardening rule for powder materials. International Journal of Mechanical Sciences 47 (1), 94–109.

Kim, K. T., Choi, S. W., Park, H., 2000. Densification behavior of ceramic powder under cold compaction. Journal of engineering materials and technology 122, 238–244.

Le, T. H., Dormieux, L., Jeannin, L., Burlion, N., Barthélémy, J.-F., 2008. Nonlinear behavior of matrix-inclusion composites under high confining pressure: application to concrete and mortar. Comptes Rendus Mécanique 336, 670–676.

28

Lee, J. W., Kim, H. W., Ku, H. C., Yoo, W. S., 2009. Comparison of external damping models in a large deformation problem. Journal of Sound and Vibration 325, 722–741.

Liu, M., Carter, J., 2002. A structured Cam Clay model. Canadian Geotechnical Journal 39, 1313–1332.

Mesbah, A., Morel, J. C., Olivier, M., 1999. Comportement des sols fins argileux pendant un essai de compactage statique : détermination des paramètres pertinents. Materials and Structures/Matériaux et Constructions 32, 687–694.

Michrafy, A., Diarra, H., Dodds, J., 2009. Compaction behavior of binary mixtures. Powder Technology 190 (1-2), 146–151.

Michrafy, A., Dodds, J., Kadiri, M., 2004. Wall friction in the compaction of pharmaceutical powders: measurement and effect on the density distribution. Powder Technology 148 (1), 53–55.

Mosbah, P., Bouvard, D., Ouedraogo, E., Stutz, P., 1997. Experimental techniques for analysis of die pressing and ejection of metal powder. Powder Technology 40, 269–277.

Nugent, E. E., Calhoun, R. B., Mortensen, A., 2000. Experimental investigation of stress and strain fields in a ductile matrix surrounding an elastic inclusion. Acta Materialia 48 (7), 1451–1467.

Olmo, C. D., Fioravante, V., Gera, F., Hueckel, T., Mayor, J., Pellegrini, R., 1996. Thermomechanical properties of deep argillaceous formations. Engineering Geology 41 (1-4), 87–102.

29

Park, J., 2007. A yield function for copper powder in compaction. Journal of Materials Processing Technology 187-188, 672–675.

Park, S.-J., Han, H. N., Oh, K. H., Lee, D. N., 1999. Model for compaction of metal powders. International Journal of Mechanical Sciences 41 (2), 121–141.

Piat, R., Reznik, B., Schnack, E., Gerthsen, D., 2004. Modeling of effective material properties of pyrolytic carbon with different texture degrees by homogenization method. Composites Science and Technology 64 (13-14), 2015–2020.

Piccolroaz, A., Bigoni, D., Gajo, A., 2006. An elastoplastic framework for granular materials becoming cohesive through mechanical densification. Part I - small strain formulation. European Journal of Mechanics - A/Solids 25 (2), 334–357.

Piret, J., Menéndez Arias, J., Franken, M., Blumenfeld, P., 2004. Study of behaviour of cement and mass joint utilisated in aggregates of steel industry. European Commission/Technical steel research - EUR21133 EN

Roscoe, K., Burland, J., 1968. On the generalized stress-strain behaviour of wet clay. Engineering Plasticity, Heyman J., Leckie F.A. (eds.), Cambridge University Press, 535–609.

Salençon, J., 2007. Mécanique des milieux continus. Tome II. Éditions de l'École Polytechnique, Palaiseau, Ellipses Paris.

Shima, S., Oyane, M., 1976. Plasticity theory for porous metals. International Journal of Mechanical Sciences 18 (6), 285–291.

30

647 Sinka, I. C., Cunningham, J. C., Zavaliangos, A., 2003. The effect of wall
648 friction in the compaction of pharmaceutical tablets with curved faces: a
649 validation study of the Drucker-Prager Cap model. Powder Technology
650 133 (1-3), 33–43.

651 Sultan, N., Delage, P., Cui, Y. J., 2002. Temperature effects on the volume
652 change behaviour of boom clay. Engineering Geology 64 (2-3), 135–145.

653 Tanaka, N., Graham, J., Lingnau, B.E., 1995. A thermal elastic plastic model
654 based on Modified Cam Clay. 10th PanAmerican Conference on Soil Me-
655 chanics and Foundations Engineering, Guadalajara, Mexico.

656 Wu, C.-Y., Ruddy, O., Bentham, A., Hancock, B., Best, S., Elliott, J., 2005.
657 Modelling the mechanical behaviour of pharmaceutical powders during
658 compaction. Powder Technology 152 (1-3), 107–117.

31

List of Figures

List of Tables

33

Figure 1: Triaxial compression test.

Figure 2: Triaxial tests with $|\sigma_R| = 200$ kPa at different temperatures and velocities.
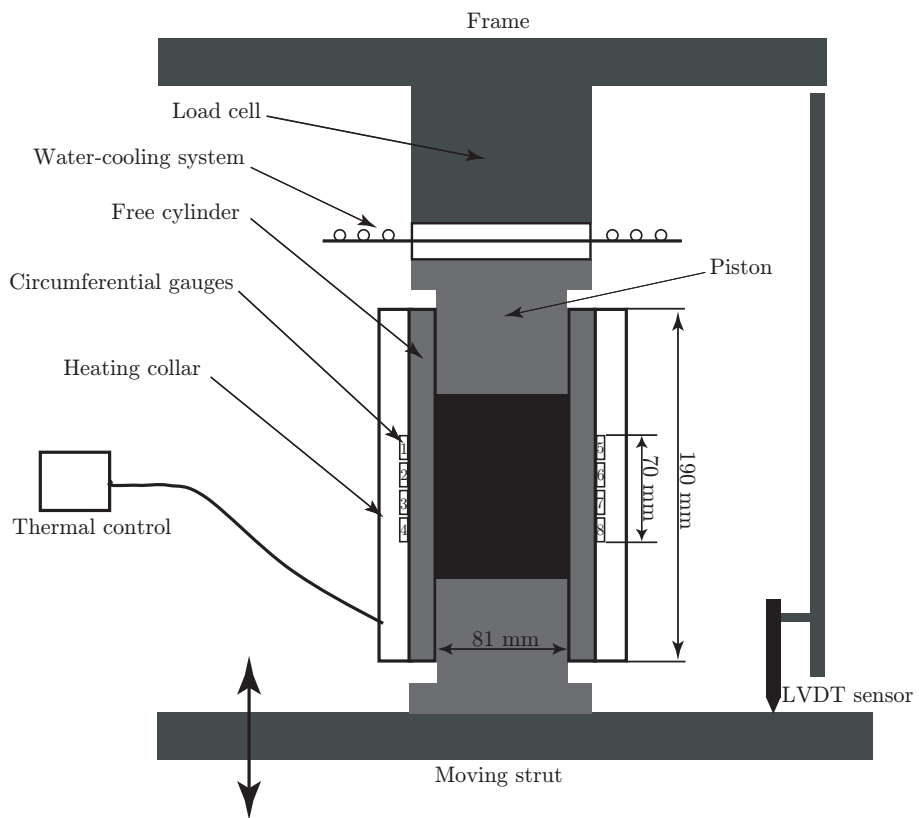
Figure 3: Instrumented die compaction test.
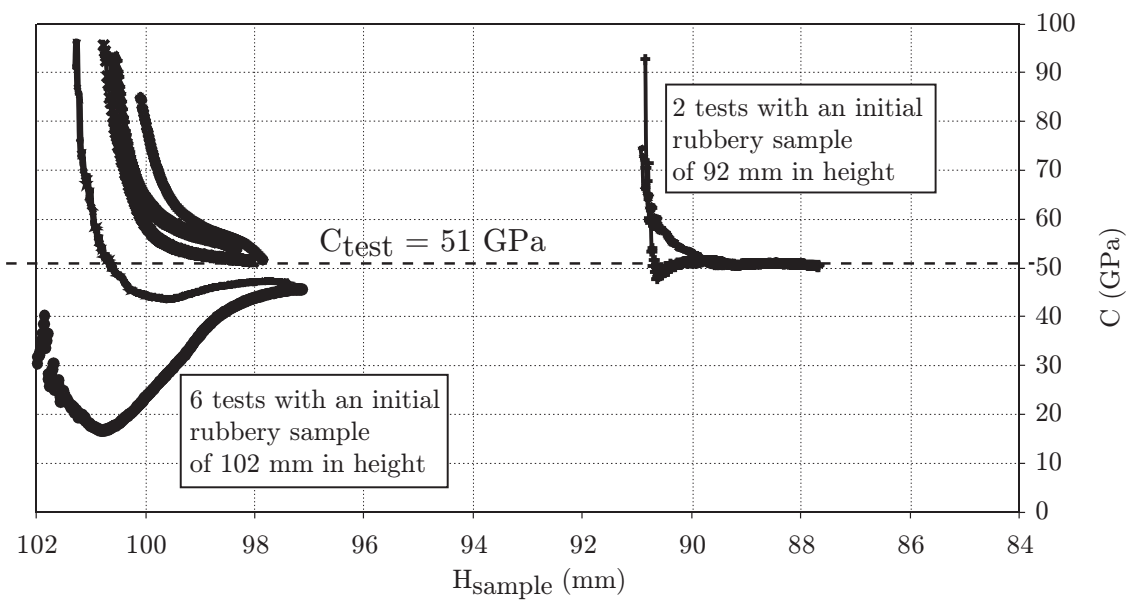
Figure 4: Identification of the calibration relation.
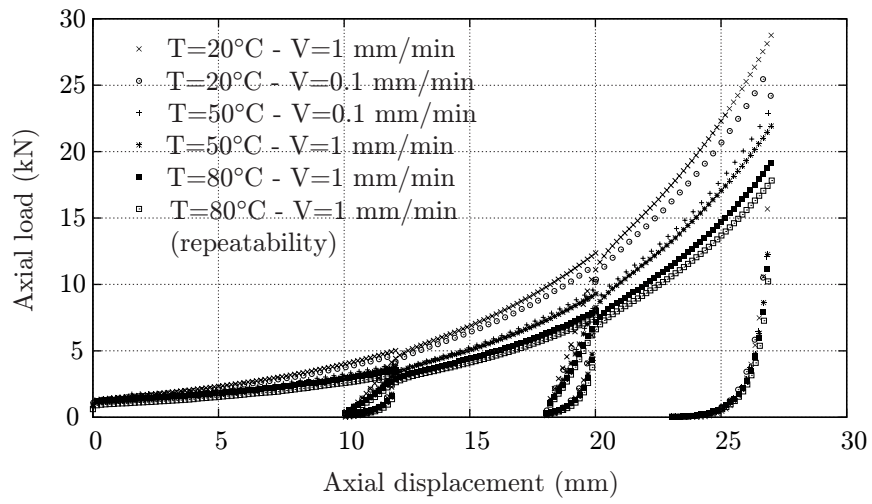
Figure 5: Results of die compaction tests at different velocities and temperatures.
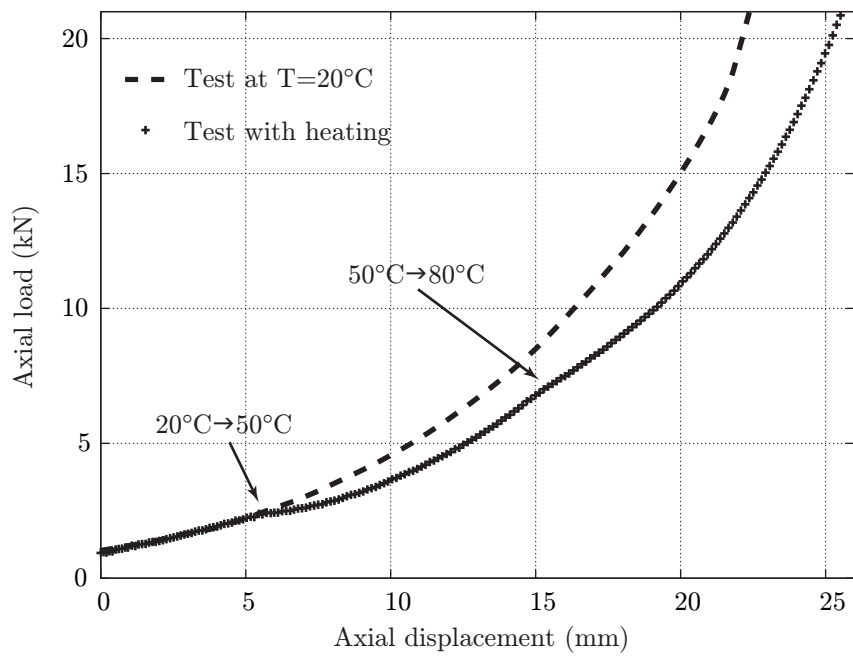
Figure 6: Temperature effect on the hardening behaviour.
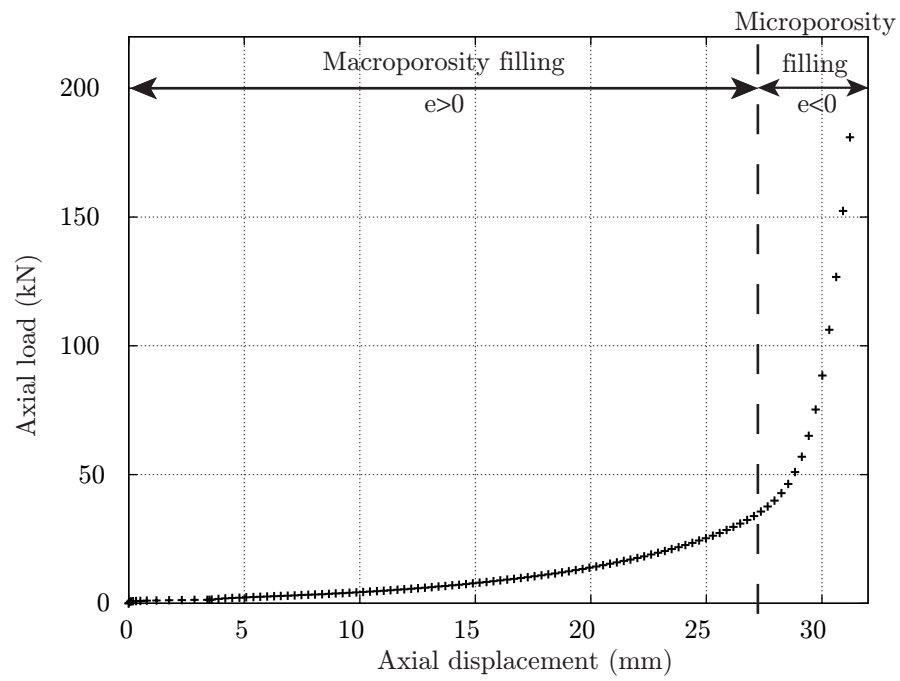
Figure 7: Die compaction test under high pressures.
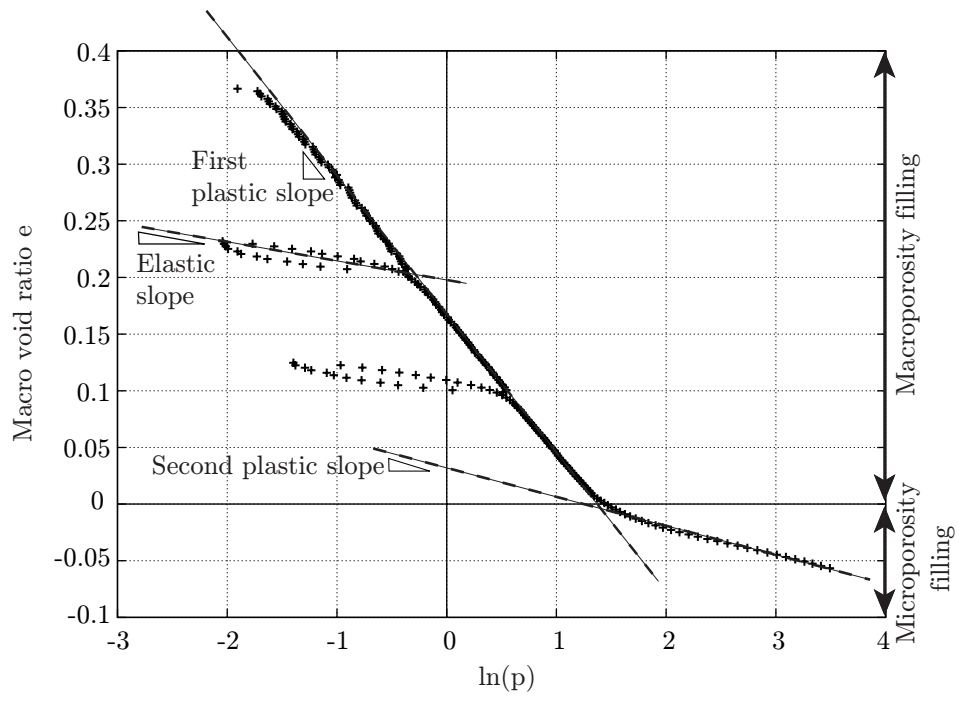
Figure 8: Hardening behaviour in the $(p,\ q)$ plane.
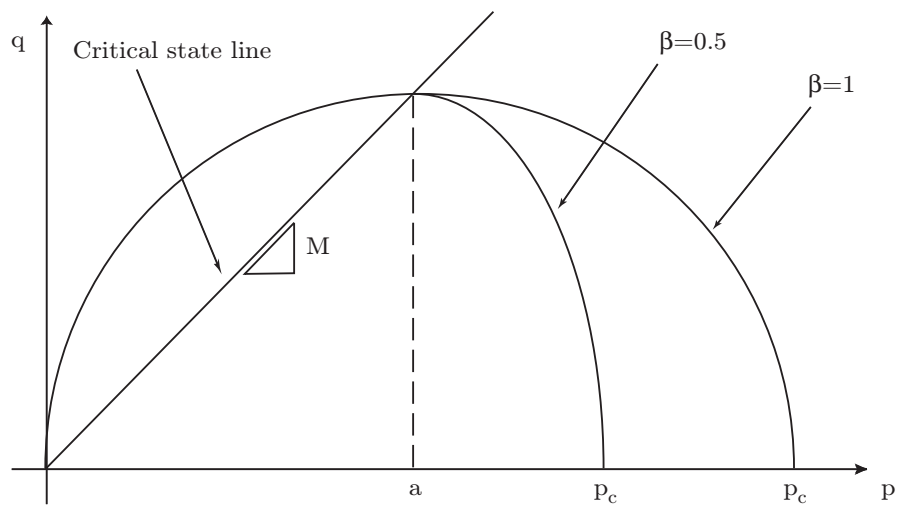
Figure 9: Yield surface and critical state line of the Modified Cam-Clay model.
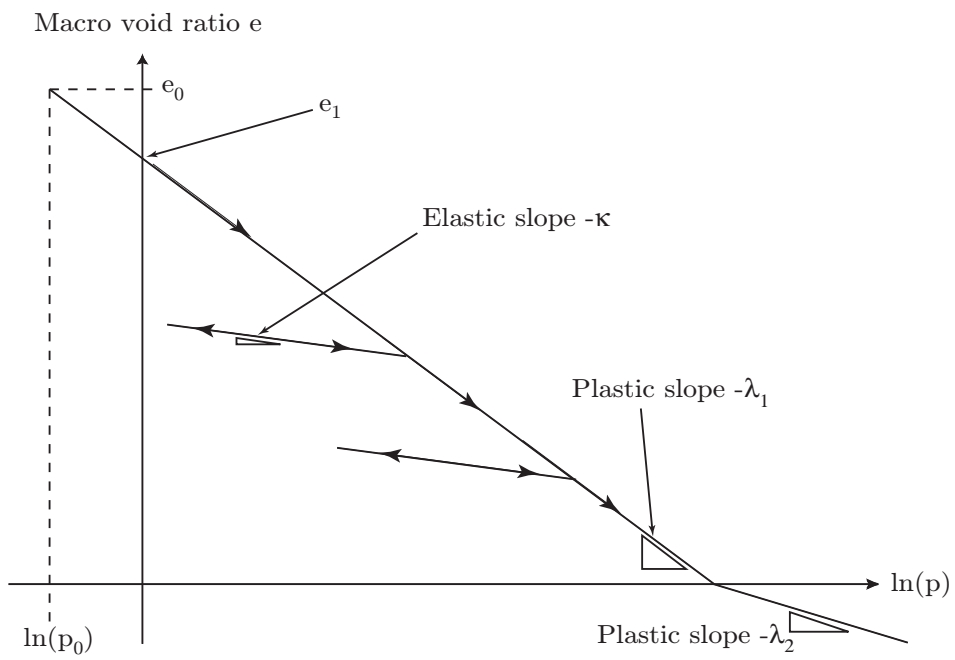
Figure 10: Compaction behaviour of the Modified Cam-Clay model.
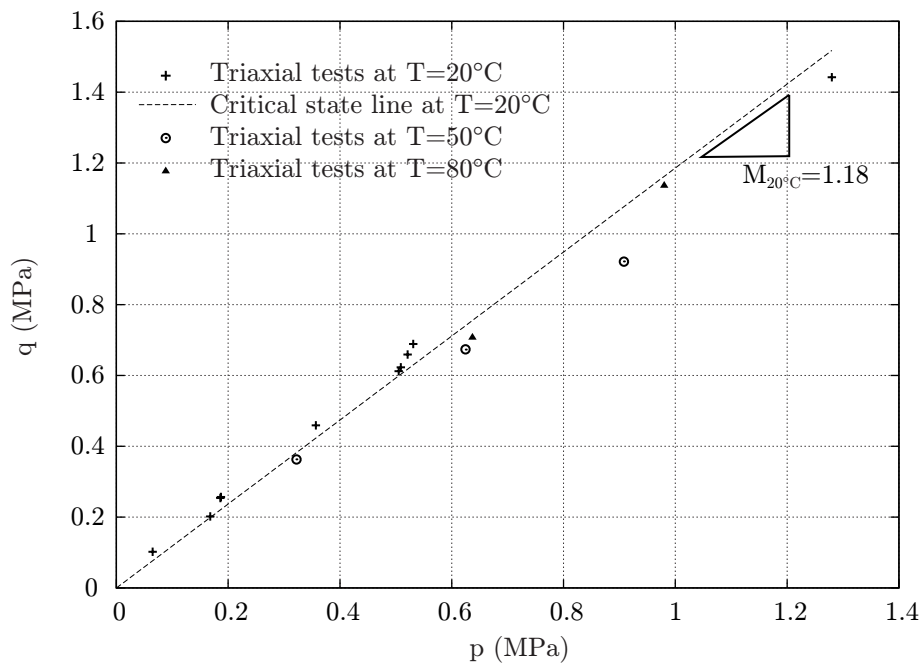
Figure 11: Results of triaxial tests at 3 different temperatures.
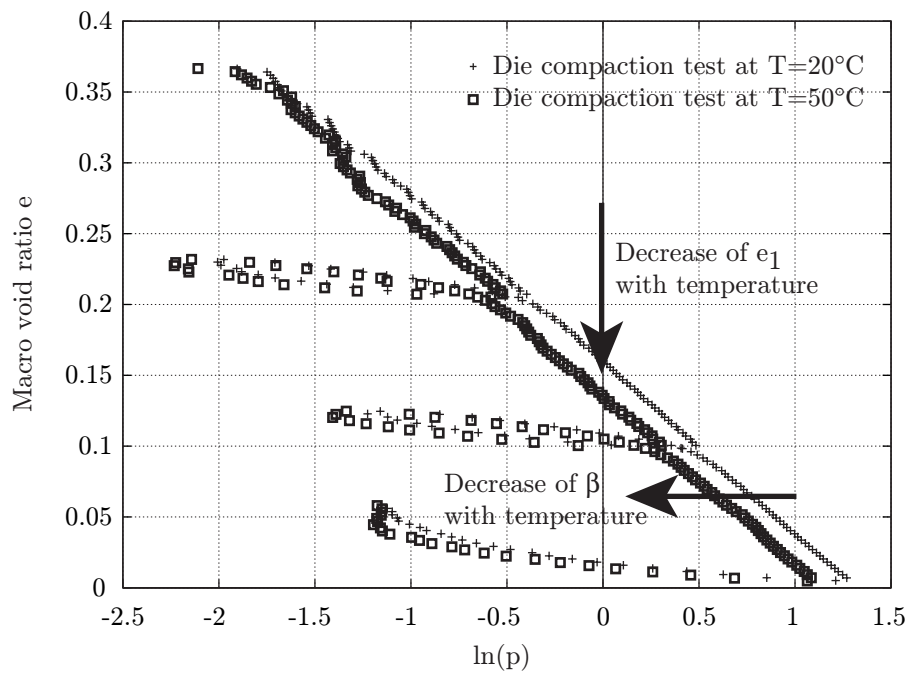
Figure 12: Influence of the temperature on the hardening behaviour.
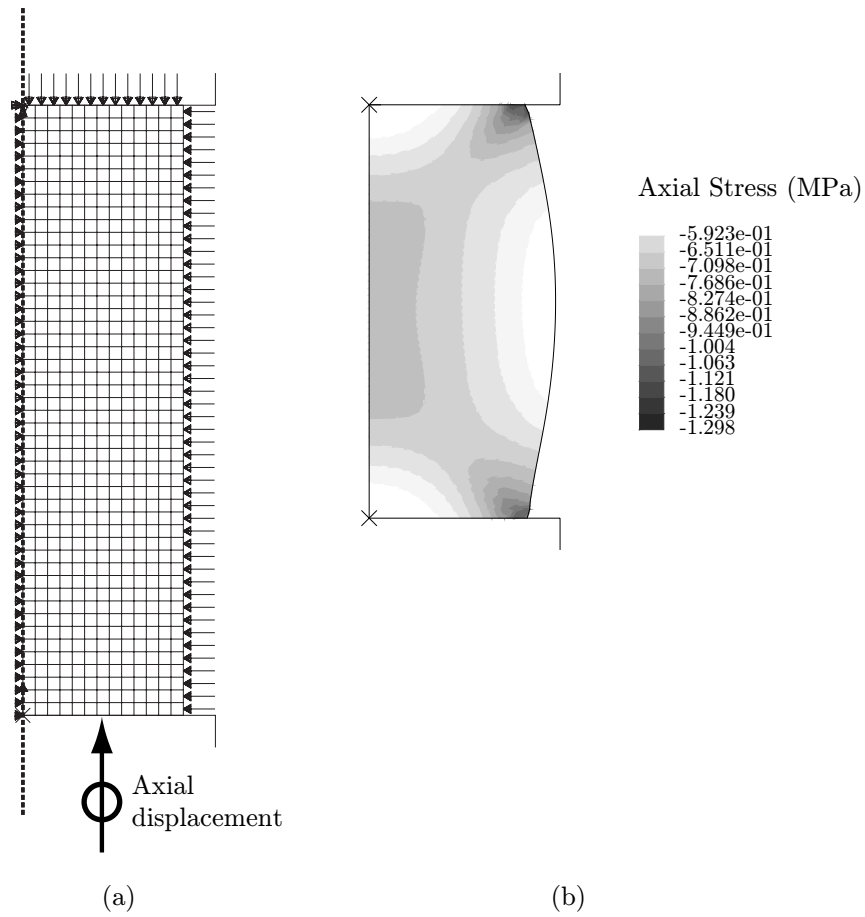
Figure 13: Simulation of the triaxial test: (a) Mesh and boundary conditions, (b) Axial stress distribution.
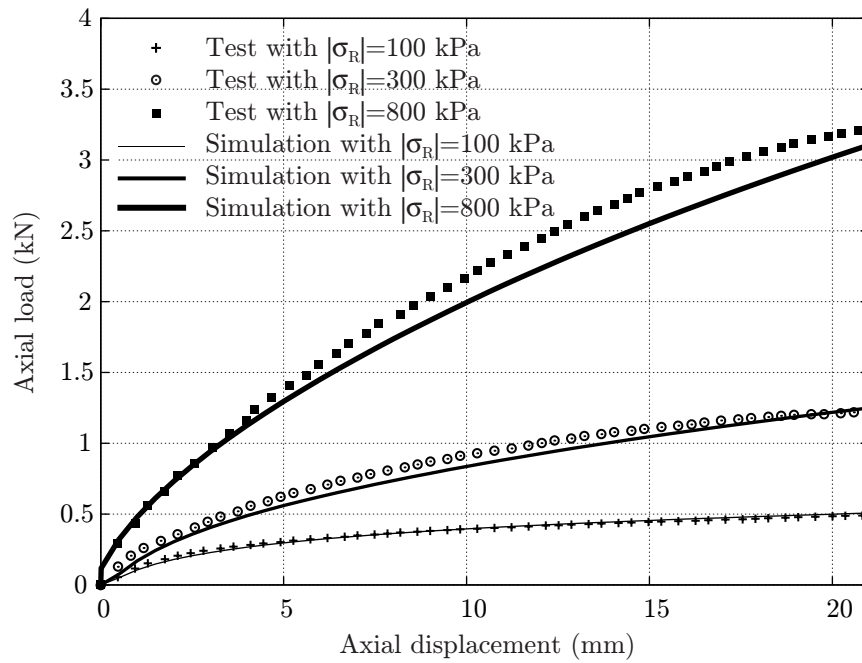
Figure 14: Triaxial tests with different radial stresses at T=20°C.
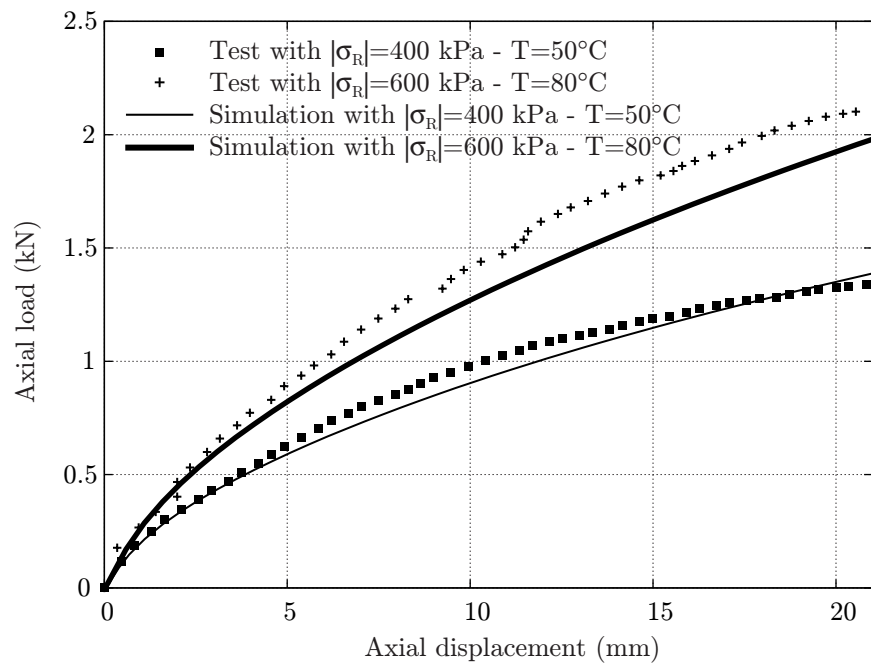
Figure 15: Triaxial tests at T=50°C and T=80°C.

Radial Stress (MPa)
+1.061e-01
+1.971e-02
-6.670e-02
-1.531e-01
-2.395e-01
-3.260e-01
-4.124e-01
-4.988e-01
-5.852e-01
-6.716e-01
-7.580e-01
-8.444e-01
-9.309e-01

Axial
displacement

(a)   (b)
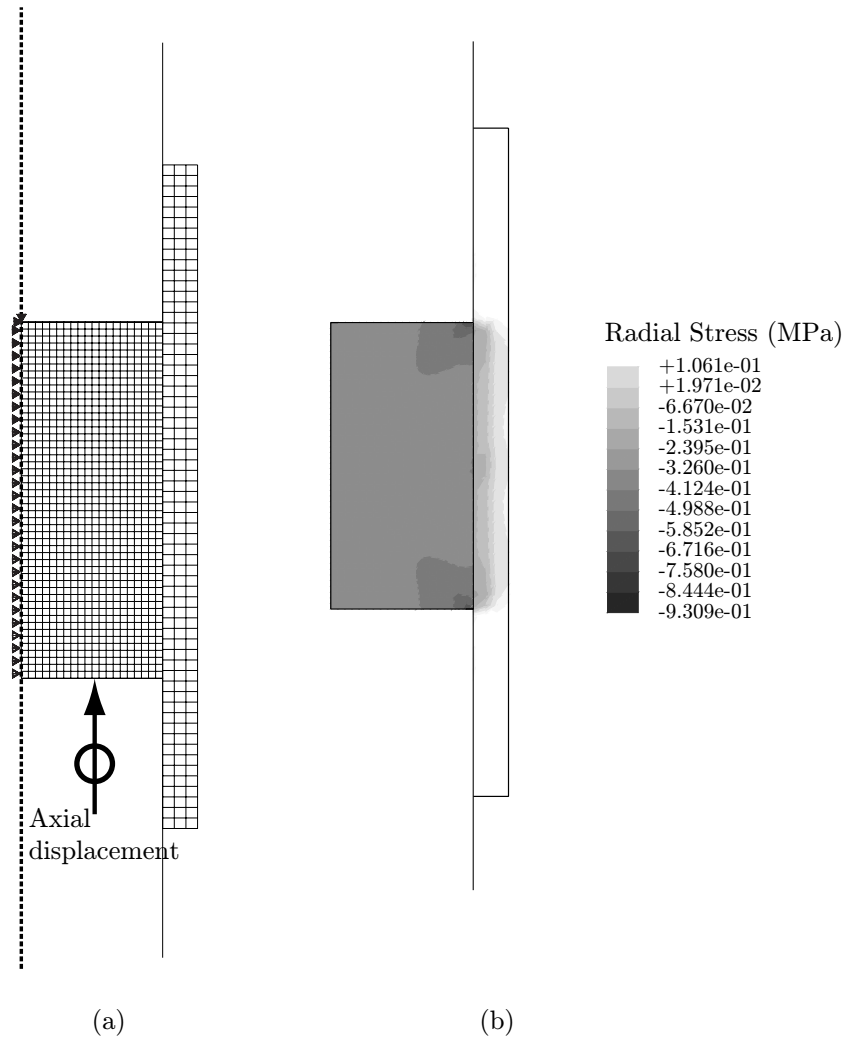
Figure 16: Simulation of the die compaction test: (a) Mesh and boundary conditions, (b) Radial stress distribution.

49
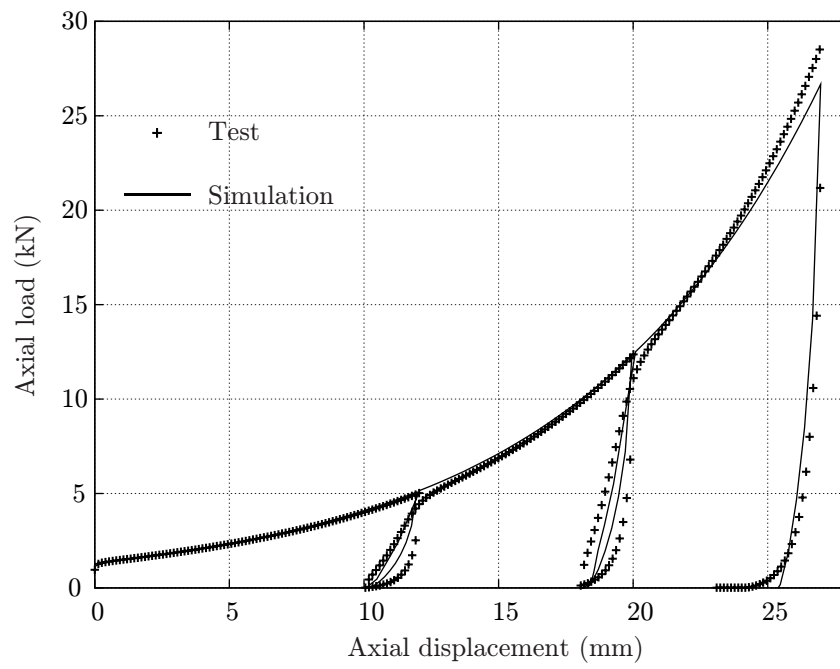
Figure 17: Die compaction test at T=20°C.
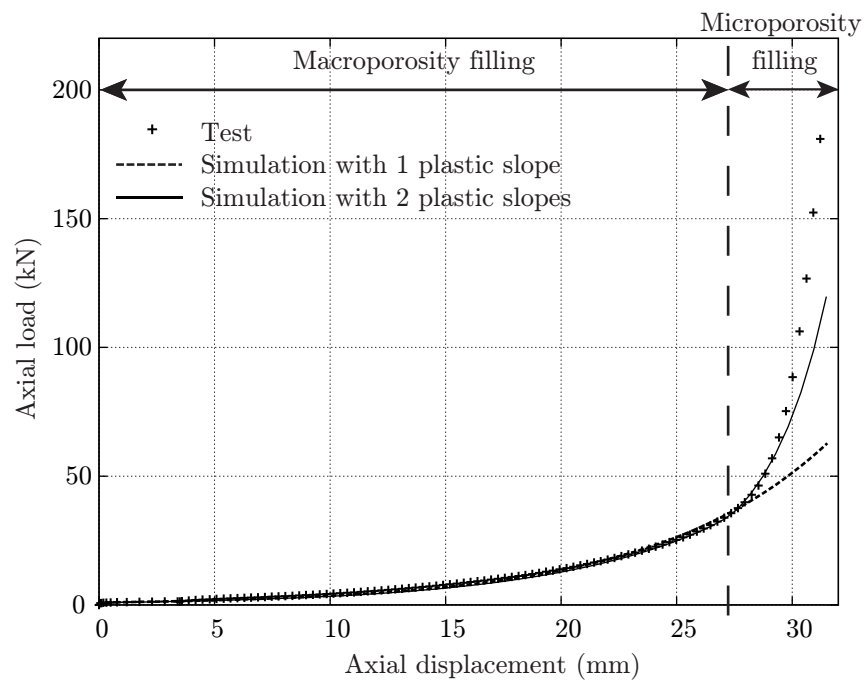
Figure 18: Experimental and numerical results for high pressures.
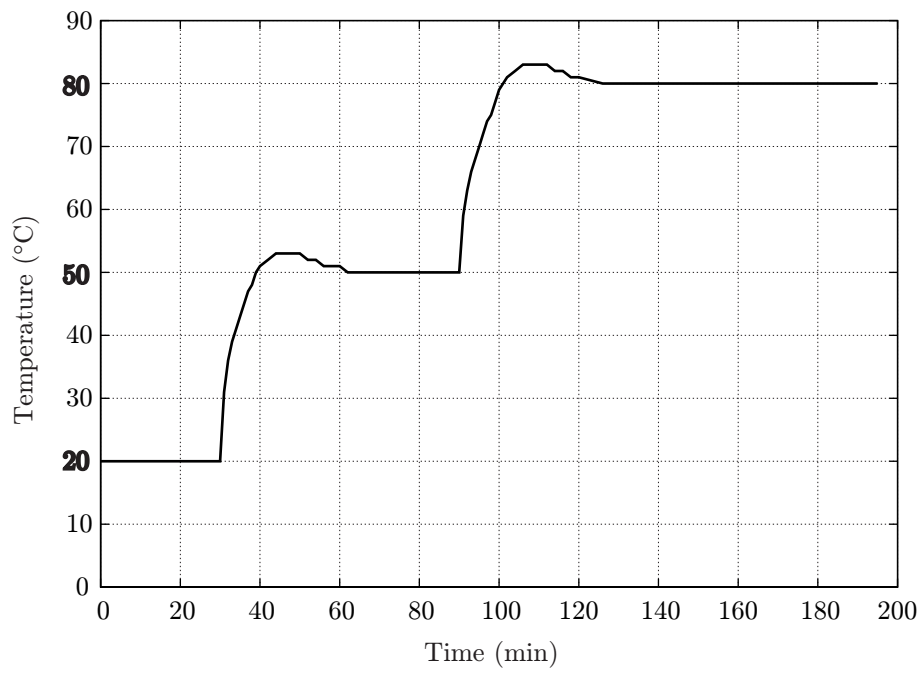
Figure 19: Temperature evolution during the die compaction test.
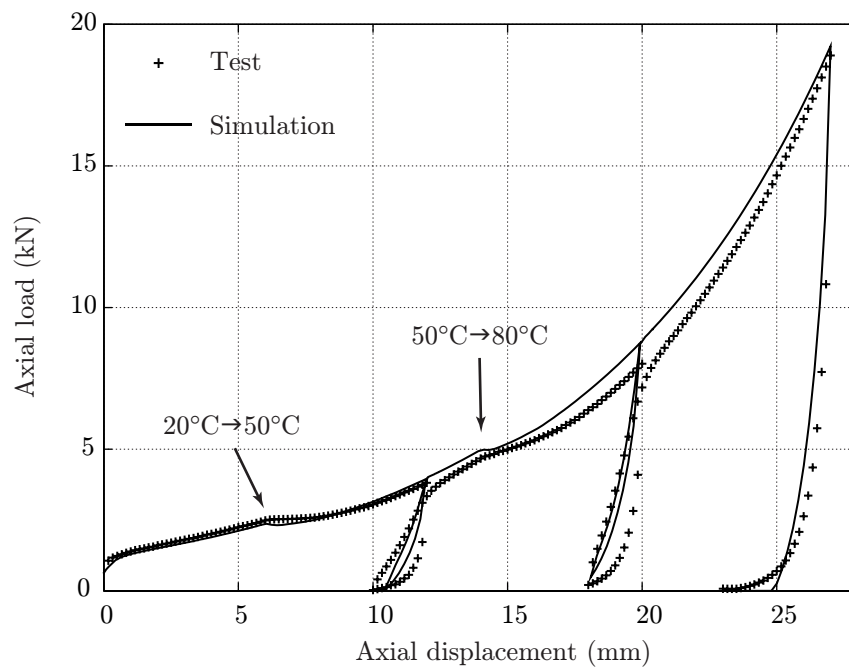
Figure 20: Die compaction test with loads/unloads and heating.
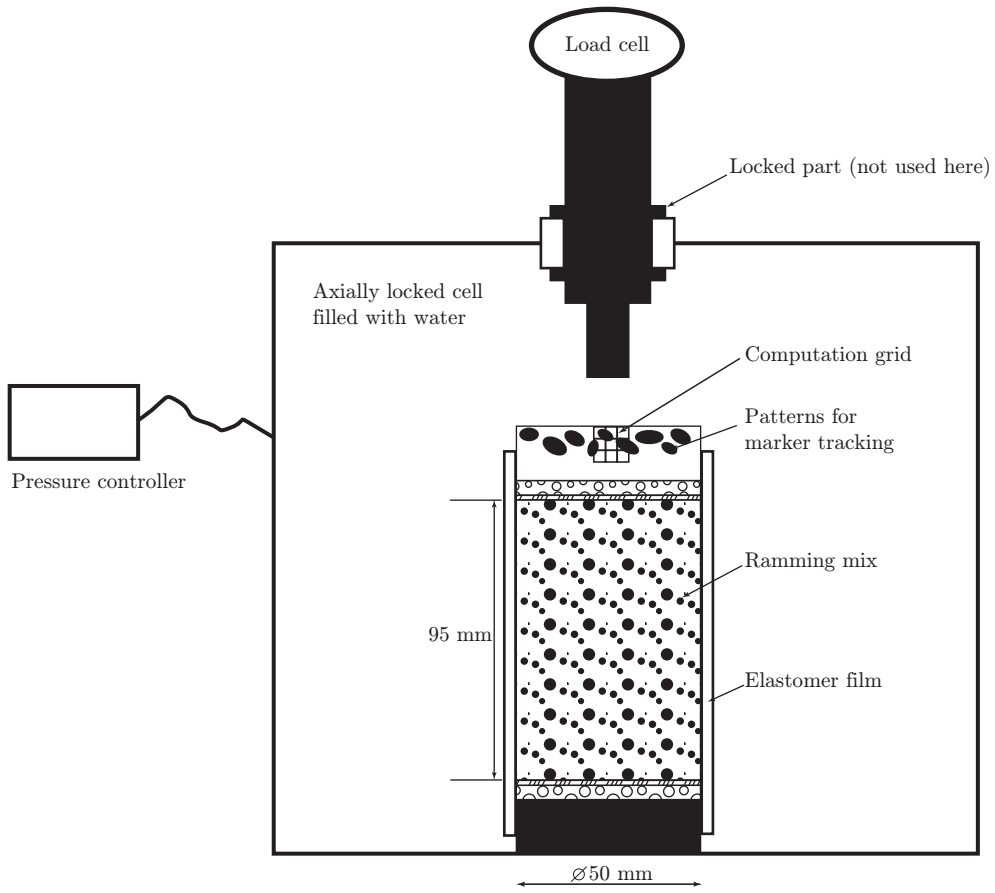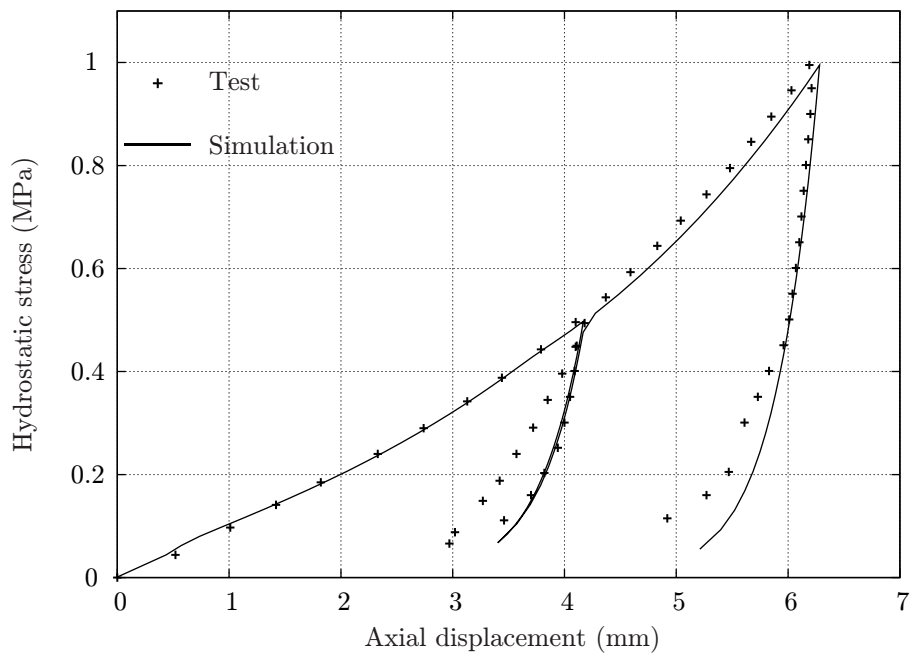
Figure 21: Hydrostatic compression test.

Figure 22: Hydrostatic compression test with loads/unloads.

Table 1: Hardening behaviour parameters.

Temperature (°C)	20	50	80
κ	0.017	0.017	0.017
λ_1	0.12	0.12	0.12
λ_2	0.024	0.024	0.024
e_1	0.16	0.13	0.1

Table 2: Modified Cam-Clay model parameters.

Temperature (°C)	20	50	80
ν		0.25	
κ		0.017	
M	1.18	1.1	1.1
λ_1		0.12	
λ_2		0.024	
e_1	0.16	0.13	0.1
β	1	0.56	0.21

Table 3: Thermal properties.

	Steel	Ramming mix
Density (kg.mm^{-3})	7.85×10^{-6}	$[1.33 \times 10^{-6}; 1.73 \times 10^{-6}]$
Conductivity (W.mm^{-1}.K^{-1})	0.047	0.025
Specific heat (J.kg^{-1}.K^{-1})	450	700
Expansion (K^{-1})	1.2×10^{-5}	3.3×10^{-6}